14. D. Yu, C. Wang, P. Guyot-Sionnest, *Science* **300**, 1277 (2003).
15. D. Yu, C. Wang, B. L. Wehrenberg, P. Guyot-Sionnest, *Phys. Rev. Lett.* **92**, 216802 (2004).
16. Materials and methods are available as supporting material on *Science* Online.
17. G. Allan, C. Dellerue, *Phys. Rev. B* **70**, 245321 (2004).
18. C. H. Ben-Porat, O. Chernyavskaya, L. Brus, K.-S. Cho, C. B. Murray, *J. Phys. Chem. B* **108**, 7814 (2004).
19. The possibility of hole injection into the $1S_h$ state of a semiconductor nanocrystal has been demonstrated by Wehrenberg and Guyot-Sionnest (*25*).
20. O. L. Lazarenkova, A. A. Balandin, *J. Appl. Phys.* **89**, 5509 (2001).
21. D. V. Talapin, A. L. Rogach, A. Kornowski, M. Haase, H. Weller, *Nano Lett.* **1**, 207 (2001).
22. J. S. Steckel, S. Coe-Sullivan, V. Bulović, M. B. Bawendi, *Adv. Mater.* **15**, 1862 (2003).
23. D. V. Talapin, unpublished data.
24. C. Klinke, J. Chen, A. Afzali, Ph. Avouris, *Nano Lett.* **5**, 555 (2005).
25. B. L. Wehrenberg, P. Guyot-Sionnest, *J. Am. Chem. Soc.* **125**, 7806 (2003).
26. We thank C. T. Black, C. R. Kagan, J. J. Urban, E. V. Shevchenko, V. Perebeinos, R. L. Sandstrom, and A. Afzali for helpful comments, suggestions, and stimulating discussions.

Supporting Online Material
www.sciencemag.org/cgi/content/full/310/5745/86/DC1
Materials and Methods
Figs. S1 to S8

28 June 2005; accepted 1 September 2005
10.1126/science.1116703

Nanoscale Imaging of Buried Structures via Scanning Near-Field Ultrasound Holography

Gajendra S. Shekhawat[1,2] and Vinayak P. Dravid[1,2,3]*

A nondestructive imaging method, scanning near-field ultrasound holography (SNFUH), has been developed that provides depth information as well as spatial resolution at the 10- to 100-nanometer scale. In SNFUH, the phase and amplitude of the scattered specimen ultrasound wave, reflected in perturbation to the surface acoustic standing wave, are mapped with a scanning probe microscopy platform to provide nanoscale-resolution images of the internal substructure of diverse materials. We have used SNFUH to image buried nanostructures, to perform subsurface metrology in microelectronic structures, and to image malaria parasites in red blood cells.

Nondestructive real-space imaging of deeply buried or embedded structures and features with lateral resolution below ~100 nm is a formidable challenge (*1*–*5*). Conventional imaging with noninvasive radiation, such as light and acoustic waves, cannot achieve useful resolution below 100 nm because of the classical diffraction limit (*6*–*8*). Scanning probe microscopy (SPM) and its analogs offer superb spatial resolution but are sensitive only to surface or shallow subsurface features (*9*, *10*). Near-field scanning optical microscopy offers subwavelength resolution but is unable to image optically opaque and deeply buried structures (*11*, *12*). Thus, with respect to nondestructive real-space imaging, there is a clear void between the two ranges of length scales offered by confocal/photon or acoustic/sonography techniques (micrometer scale) (*13*–*16*) and SPM (nano- and subnanometer scale) (*9*, *10*), particularly if the features of interest are buried deeper into the material, beyond the interaction range of proximal probes.

The need for nondestructive nanoscale imaging of buried and embedded structures is critical for numerous materials, structures, and phenomena as the scale of fabrication continues to shrink and the micro/nanofabrication paradigm moves from planar to three-dimensional (3D) or stacked platforms. In microelectronics, for example, such metrology challenges are well articulated in the International Technology Roadmap for Semiconductors (*17*). The need for a higher resolution, nondestructive, real-space imaging approach is equally critical in biological systems for noninvasive monitoring of signal pathways, cellular transfection, and other subcellular phenomena.

In conventional nondestructive imaging approaches based on acoustic and light microscopy, classical diffraction limits the spatial resolution in the far-field regime. For example, the spatial resolution, δ, in an acoustic microscope is given by

$$\delta = 0.51(v_o/fNA) \quad (1)$$

(*7*, *8*), where v_o is the speed of sound in the coupling medium, f is the frequency of the acoustic/ultrasonic wave, and NA is the numerical aperture of the lens. Conventional far-field approaches are also limited by the need for liquid lenses and coupling fluid, among other considerations.

Several SPM-based techniques have been introduced in recent years with mixed results in the context of sensitivity to surface nanomechanical variations, ability to probe deeply buried or embedded features, or quantitative extraction of nanomechanical contrast. Force modulation microscopy (also called ultrasonic force microscopy) (*18*–*23*) and heterodyne force microscopy (*24*) are notable SPM-based techniques that have enjoyed some success in nanomechanical mapping of elastic and viscoelastic properties of soft and hard surfaces. However, a wider deployment of these techniques is generally marred by lack of reproducibility, unpredictable environmental effects in the usual contact mode of imaging, and lack of compelling evidence for demonstrated sensitivity to buried and embedded structure. Moreover, these techniques use nonlinear tip-sample interactions, where the origin of the dominant mechanical contrast in the images is mainly from differential surface mechanical properties with a large physical contact between the cantilever and sample; such methods are therefore not well suited for imaging of soft materials such as polymers and biological structures.

Here we introduce an imaging approach, scanning near-field ultrasound holography (SNFUH), that is sensitive to deeply buried features, offers nanoscale lateral resolution with depth sensitivity, and is equally amenable to hard (engineered systems), soft (polymers and biological structures), and hybrid materials. In SNFUH, a high-frequency acoustic wave (on the order of megahertz or higher, substantially greater than the resonance frequency of the typical cantilever, f_0 ~ 10 to 100 kHz) is launched from the bottom of the specimen while another wave is launched on the SPM cantilever, albeit at a slightly different frequency (Fig. 1). The interference of these two waves would nominally form a surface acoustic standing wave, which is analogous to, for example, x-ray standing waves that result from interference of scattered and reference x-ray waves (*25*, *26*). The perturbations to the phase and amplitude of the surface acoustic standing wave are locally monitored by the SPM acoustic antenna via the lock-in approach and a SNFUH electronic module. As the specimen acoustic wave is perturbed by buried features, the resultant alteration in the surface acoustic standing wave, especially its phase, is effectively monitored by the SPM cantilever. Thus, within the near-field regime (which enjoys superb spatial resolution), the acoustic wave (which is nondestructive and sensitive to mechanical and/or elastic variation along its path) is fully analyzed, point-by-point, by the SPM acoustic antenna in terms of its phase and amplitude. Thus, as the specimen is scanned, a pictorial representation of its acoustic wave perturbation is recorded and displayed that offers a quantitative account of the internal features of the specimen.

[1]Institute for Nanotechnology, [2]NU*ANCE* Center, [3]Department of Materials Science and Engineering, Northwestern University, Evanston, IL 60208, USA.

*To whom correspondence should be addressed. E-mail: v-dravid@northwestern.edu

The SNFUH approach, especially its implementation, is quite different from prior approaches (*18*–*24*) that make use of launching ultrasound frequency on the specimen, the cantilever, or both. The difference is in the collective combination of near-field, noncontact, and holography mode for detection, with noninvasive acoustic waves for depth sensitivity, as demonstrated below.

A conventional JEOL SPM 5200 scanning probe microscope system with a modified stage and cantilever holder system was used to develop the SNFUH mode. The feedback electronics of the system were also modified, and an electronic module developed in-house was implemented together with a radio frequency (RF) lock-in approach to extract the phase and amplitude of the acoustic standing wave perturbed by buried features. Commercial piezoelectric ceramics were used to provide ultrasonic vibrations to the sample and the cantilever, with out-of-plane resonances of ~2.1 and ~2.3 MHz, respectively. The images were acquired using soft-contact mode (for hard structures) and near-contact mode (for biological structures). In soft-contact mode, the SNFUH feedback controller is used to bring the cantilever toward the surface, and the contact force is monitored by the system software. In near-contact mode, optical feedback is used to lift the tip by a small amount (2 to 5 nm) after it touches the surface.

The SNFUH controller and cantilever monitor the perturbation to the surface acoustic standing waves, especially their phase, which carries information about buried structures reflected in the scattering of specimen acoustic waves due to the difference in elastic moduli, for example. The use of near-contact mode is particularly suitable for imaging and monitoring soft and biological structures in vitro. Matching piezoceramics were used to keep the frequency difference below the cutoff frequency of the SPM photodiode (~1 MHz). The SPM differential photodiode signal constitutes an input to the SNFUH electronic module, which enables simultaneous extraction of all image data: the topography, amplitude, and phase of the acoustic standing wave.

Experimentally, the two acoustic oscillations are applied to the tip and the sample by two matching piezocrystals attached to the cantilever and at the base of the sample. Each piezocrystal is driven by a separate sinusoidal waveform generated by arbitrary waveform generators. The SNFUH electronic module monitors the difference frequency input to an RF lock-in amplifier as a reference for the extraction of the amplitude phase of the acoustic standing wave.

We used a model polymer-nanoparticle composite to demonstrate the high lateral spatial resolution and depth sensitivity of the SNFUH approach. A specimen consisting of gold nanoparticles buried deep beneath a polymer cover layer was prepared by dispersing colloidal gold nanoparticles on a silicon substrate coated with poly(2-vinylpyridine) (PVP). Nanoparticle coverage was measured by Rutherford backscattering spectrometry as described (*27*). The gold nanoparticles had an average diameter of 15 nm and were well dispersed on the film surface, as observed previously by transmission electron microscopy (TEM) (*27*). The nanoparticles were then fully covered with another polymer film about 500 nm thick (Fig. 2A). The normal atomic force microscopy (AFM) topography scan (Fig. 2B) shows a smooth featureless surface of top polymeric layer with surface roughness of ~0.5 nm. However, the phase image of SNFUH (Fig. 2C) clearly shows well-dispersed gold nanoparticles buried ~500 nm deep from the top surface. The contrast in the phase image of SNFUH arises from the difference in elastic modulus between the polymer and the gold nanoparticles, which induces the time-dependent phase delay of the acoustic waves reaching the sample surface.

As shown schematically in Fig. 2, D and E, the buried scattering features (the nanoparticles) perturb the specimen acoustic wave, resulting in local change in the phase and amplitude of the acoustic standing wave, which is detected by the SPM cantilever "antenna." At the operating frequency of 2.1 MHz, the wavelength of the specimen acoustic wave is greater than a few hundred micrometers. Thus, the experimental conditions are well within the near-field regime, resulting in minimal diffraction or wide-angle scattering of the acoustic waves reaching the top surface. The degradation of spatial resolution and the depth sensitivity of SNFUH beyond the near-field regime requires additional experimental and modeling studies.

The mechanism of the formation of the acoustic standing wave and the origin of the contrast and high subsurface sensitivity of the SNFUH approach can be conceptually understood as follows (Fig. 2, D and E): In SNFUH mode, the perturbation to the surface acoustic standing wave resulting from specimen

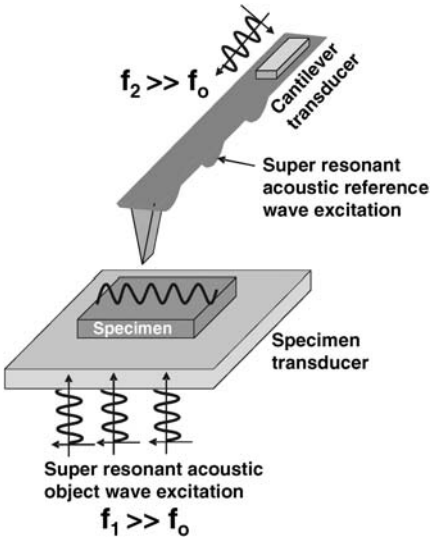

Fig. 1. Schematic illustration of the SNFUH approach. A high-frequency acoustic wave is launched from below the specimen while another high-frequency acoustic wave (at a slightly different frequency) is launched on the SPM cantilever. The SNFUH electronic module is used to spatially monitor the phase perturbation to the surface acoustic standing wave that results from the scattered specimen acoustic wave. The resonant frequency of the typical cantilever, f_o, is in the 10- to 100-kHz range.

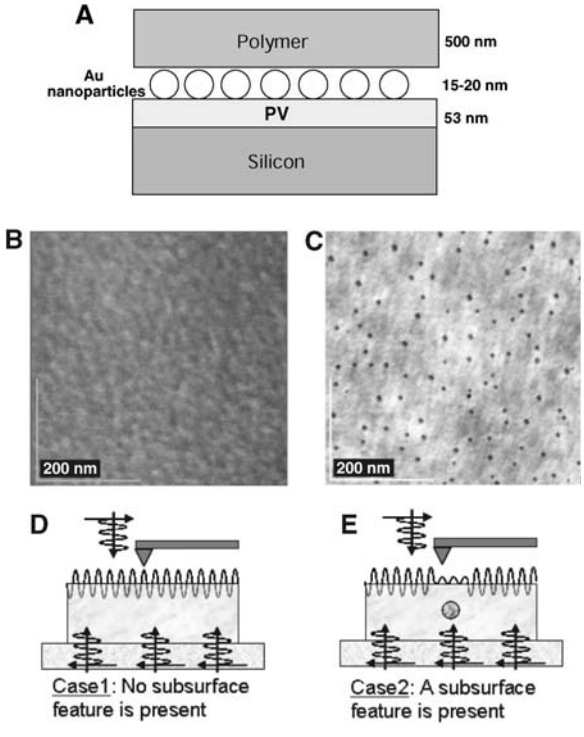

Fig. 2. (**A**) Schematic illustration of a model nanoparticle system for validation of SNFUH. Gold nanoparticles dispersed on a polymer-coated substrate (PV) are buried under a polymer layer ~500 nm thick. (**B** and **C**) A typical AFM topography image (B) shows a featureless top polymer surface, whereas the phase image of SNFUH (C) clearly reveals the buried gold nanoparticles with high definition. (**D** and **E**) Schematic explanation of images in (B) and (C). In (D), the standing wave is not perturbed because no subsurface scattering feature is present; in (E), the acoustic standing wave is perturbed as a result of subsurface scattering, which is monitored by the SPM tip.

acoustic wave scattering is monitored by the SPM acoustic antenna. The resulting cantilever deflection merely follows the perturbation to the surface acoustic standing wave, which represents the dissipative lag/lead in the surface response with respect to the tip reference frequency (i.e., the time-of-flight delay of the specimen acoustic waves reaching the sample surface). Extracting the spatial dependence of this phase term provides image contrast indicative of the relative elastic response of the buried structures, interfaces, and embedded defects to the specimen acoustic wave to create the resultant perturbation to the surface acoustic standing wave.

In a homogeneous specimen, the surface acoustic standing wave is merely the interference of the specimen and cantilever acoustic waves without any local perturbation (Fig. 2D). However, if a scattering feature is present below the specimen surface, the perturbation to the specimen acoustic wave results in local perturbation (Fig. 2E) to the surface acoustic standing wave that is registered by the SPM cantilever antenna. The contrast variation arises from the acoustic phase difference between the matrix and the feature, which in the case of acoustic wave propagation is directly related to the elastic modulus difference (*7*, *8*). The lateral spatial resolution is governed by the SPM probe interaction with the acoustic standing wave, which is proportional to the depth of the scattering features beyond the near-field regime. Within the near-field regime, the spatial resolution is limited principally by the SPM tip interactions, whereas resolution degradation will be commensurate with depth beyond the near-field regime because of far-field scattering and diffraction. Further, because the acoustic phase information is spatially recorded, it is possible to obtain (via modeling) depth distribution of phase and to convert the data into a 3D tomography map of the embedded features.

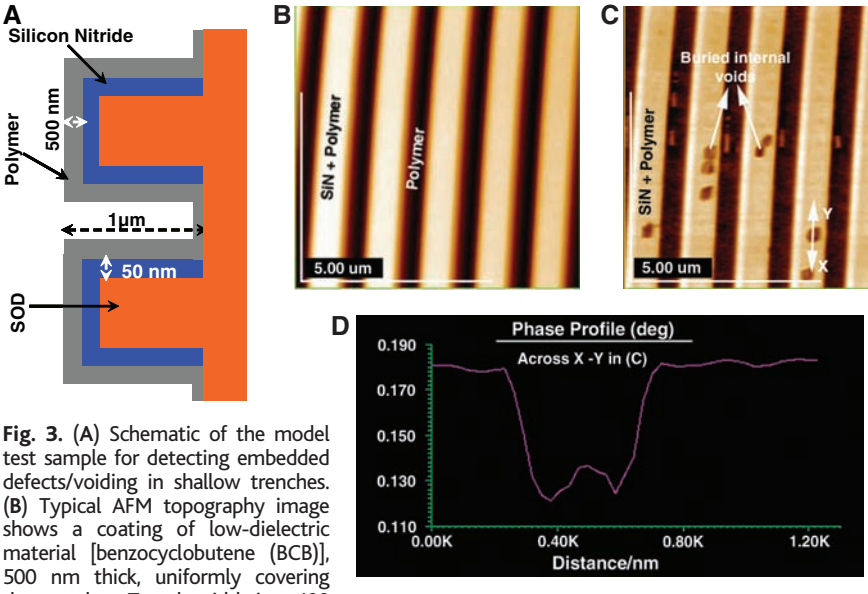

Fig. 3. (**A**) Schematic of the model test sample for detecting embedded defects/voiding in shallow trenches. (**B**) Typical AFM topography image shows a coating of low-dielectric material [benzocyclobutene (BCB)], 500 nm thick, uniformly covering the trenches. Trench width is ~400 nm and height is ~1 μm. (**C**) Phase image of SNFUH clearly reveals the surface elastic contrast and embedded voiding in polymer coating over nitride and hardening of it at the trench walls, a result of its curing. This is evident from the contrast at the trench walls. (**D**) The line profile across the void, marked across X-Y in (C). Remarkably high subsurface phase resolution is achieved.

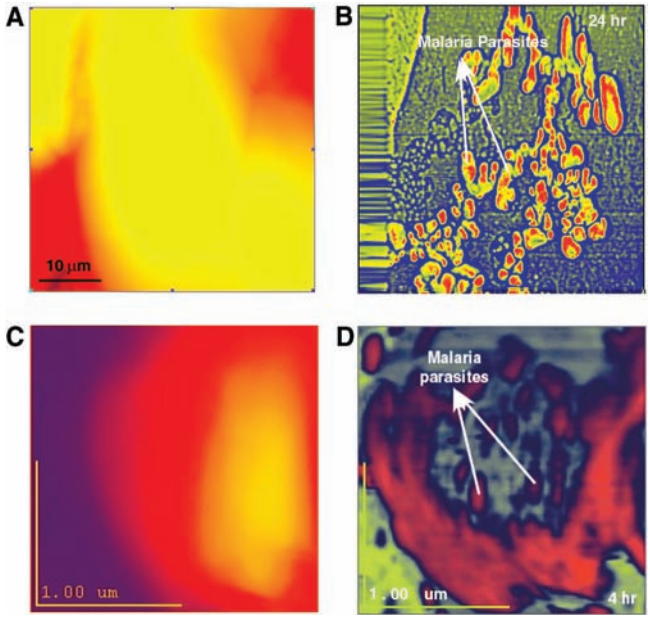

Fig. 4. AFM topography images (**A** and **C**) and SNFUH phase images (**B** and **D**) of malaria-infected RBCs. In (A) and (B), obtained after 24 hours of incubation, the topography image shows typical surface features of RBCs with scan size of 10 μm by 10 μm, whereas the SNFUH phase image shows remarkable contrast from parasites inside the RBC at nanoscale spatial resolution. The images in (C) and (D) show early-stage parasite infection after 4 hours of incubation.

Some of the challenges in the next generation of microelectronics metrology include dimensionality and fatigue performance of electrical contacts and interconnects (*28*, *29*), which are often buried and stacked. The current paradigm for electrical contact processing calls for an increase in the aspect ratio of metal contact lines, which in turn requires deposition of metal into damascene trenches and *vias* without leaving any unfilled volume (voids). The undesirable process defect voids result in increased resistivity and can cause serious open circuits and device failure. The major challenges in this critical microelectronics step include voiding, delamination, and cracking at the polymer-trench interface. Conventional techniques for characterization of voids and stresses in narrower trenches include destructive approaches such as cross-sectional scanning electron microscopy (SEM) or TEM, which are not only laborious and time-consuming but require the wafer to be sacrificed. Electrical testing is nondestructive but spatially insensitive, and it requires contact to the wafer. In the case of *via* chains, several metal levels must be fabricated before the electrical test can be completed. Clearly, a nondestructive subsurface imaging approach is warranted to identify and isolate such defects or delamination and thereby improve the process yield.

To demonstrate the efficacy of SNFUH in identifying underlying defects in narrower trenches, we fabricated shallow trench structures as shown in Fig. 3A. The trenches were etched in SOD (spin-on dielectric) with a 50-nm layer of low-pressure chemical vapor deposition (LPCVD) Si_3N_4 as a capping layer, and Si_3N_4 was then etched into the trenches (1 μm deep) by wet processing. A layer of polymer (benzocyclobutene) 500 nm thick was spin-coated, followed by thermal annealing to cure the polymer.

A conventional topography scan (Fig. 3B), 7.5 μm by 7.5 μm, shows uniform and contiguous polymeric coating on SiN and inside the trenches. On the other hand, the corresponding (simultaneously recorded) SNFUH phase image shown in Fig. 3C reveals phase contrast reminiscent of embedded voiding within the polymer and at the SiN-polymer interfaces. The dark contrast in the phase image in polymer-

coated SiN lines corresponds to voids at SiN-polymer interfaces (i.e., voiding underneath the contact). The contrast is due to the distinct viscoelastic response from the specimen acoustic wave from the voids. Interestingly, a notable hardening of the polymer in the trench and its sidewall is also evident in the phase image, which results from thermal annealing and possibly poor adhesion with SOD. Because it is nondestructive, SNFUH may be an ideal toolset for such subsurface metrology needs.

The efficacy of SNFUH in imaging of embedded or buried substructures in biology is demonstrated in Fig. 4, which depicts high resolution and remarkably high contrast arising from malaria parasites inside infected red blood cells (RBCs). The details of in vitro infection by malaria parasites are reported in (*30*); here, we demonstrate early-stage direct and real-space in vitro imaging of the presence of parasites inside RBCs without any labels or sectioning of cells, and under physiologically viable conditions. *Plasmodium falciparum* strain 3D7 was cultured in vitro by a modification of the method of Haldar *et al*. (*31*). Parasites were synchronized to within 4 hours by a combination of Percoll purification and sorbitol treatments, cultured to 10% parasitemia, and harvested at the indicated times.

SNFUH imaging was performed using the near-contact mode method for imaging soft structures. The SNFUH electronic module was used to bring the cantilever into near-contact mode, and then the sample was scanned over the RBCs while maintaining the near-field regime. An AFM topography image and a SNFUH phase image from infected RBCs are shown in Fig. 4, A and B, respectively. As expected, the AFM topography image shows the typical surface morphology of an infected RBC, whereas the SNFUH phase image shows remarkably high contrast from the parasite residing well inside the RBC. In addition to several other features reminiscent of membrane proteins and subcellular contents, multiple parasites are clearly evident. The morphology, spatial scale, and distribution of parasites are consistent with prior accounts of such infection (*30*, *32*). To further demonstrate the capability of SNFUH for early-stage diagnosis of parasite infection, we examined RBCs incubated for only 4 hours; infection after such a brief period is difficult to validate by other noninvasive techniques such as fluorescence tagging. The images in Fig. 4, C and D, show that SNFUH is sensitive to early-stage parasite infection in RBCs, as reflected by image contrast consistent with parasite infection.

These representative examples of SNFUH development and applications demonstrate a versatile toolset for nondestructive, high-resolution, real-space imaging of diverse materials systems. We believe the SNFUH approach fills the critical gap in spatial resolution at the 10- to 100-nm scale for nondestructive subsurface imaging in physical sciences, engineered systems, and biology.

References and Notes

1. H. N. Lin, *Appl. Phys. Lett.* **74**, 2785 (1999).
2. M. R. VanLandingham *et al*., in *Interfacial Engineering for Optimized Properties*, C. L. Briant, C. B. Carter, E. L. Hall, Eds., vol. 458 of *Materials Research Society Proceedings* (Materials Research Society, Pittsburgh, PA, 1997), pp. 313–318.
3. M. R. VanLandingham *et al.*, *J. Adhesion* **64**, 31 (1997).
4. B. Bhushan, L. Huiwen, *Nanotechnology* **15**, 1785 (2004).
5. M. R. VanLandingham *et al.*, *J. Mater. Sci. Lett.* **16**, 117 (1997).
6. K. Inagaki, G. A. D. Briggs, O. B. Wright, *Appl. Phys. Lett.* **76**, 1836 (2000).
7. G. A. D. Briggs, *Acoustic Microscopy* (Clarendon, Oxford, 1992), p. 33.
8. T. M. Nelson, R. W. Smith, *Adv. Mater. Process.* **162**, 29 (2004).
9. G. S. Shekhawat *et al.*, *Appl. Phys. Lett.* **68**, 779 (1996).
10. C. F. Quate, *Surf. Sci.* **299–300**, 980 (1994).
11. W. Dickson, S. Takahashi, R. Polland, R. Atkinson, *IEEE Trans. Nanotechnol.* **4**, 229 (2005).
12. K. Lindfors, M. Kapulainen, R. Ryytty, M. Kaivola, *Opt. Laser Technol.* **36**, 651 (2004).
13. B. C. Larson, W. Yang, G. E. Ice, J. D. Budai, J. Z. Tischler, *Nature* **415**, 887 (2002).
14. X. Wang, Y. J. Pang, G. Ku, G. Stoica, L. H. V. Wang, *Opt. Lett.* **28**, 1739 (2003).
15. K. Kostli, P. C. Beard, *Appl. Opt.* **42**, 1899 (2003).
16. D.-Z. Huang, J.-B. Li, Z. Sheng, *Chin. J. Med. Imaging Technol.* **20**, 1815 (2004).
17. International Technology Roadmap for Semiconductors (http://public.itrs.net).
18. B. Altemus, G. S. Shekhawat, R. Geer, B. Xu, J. Castracane, *Proc. SPIE 4558* (2001).
19. R. E. Geer, O. V. Kolosov, G. A. D. Briggs, G. S. Shekhawat, *J. Appl. Phys.* **91**, 4549 (2002).
20. O. Kolosov, R. M. Castell, C. D. Marsh, G. A. D. Briggs, *Phys. Rev. Lett.* **81**, 1046 (1998).
21. D. C. Hurley, K. Shen, N. M. Jennett, J. A. Turner, *J. Appl. Phys.* **94**, 2347 (2003).
22. O. Hirotsugu, T. Jiayong, T. Toyokazu, H. Masahiko, *Appl. Phys. Lett.* **83**, 464 (2003).
23. L. Muthuswami, R. E. Geer, *Appl. Phys. Lett.* **84**, 5082 (2004).
24. M. T. Cuberes, H. E. Assender, G. A. D. Briggs, O. V. Kolosov, *J. Phys. D* **33**, 2347 (2000).
25. L. Cheng, P. Fenter, M. J. Bedzyk, N. C. Sturchio, *Phys. Rev. Lett.* **90**, 255503-1-4 (2003).
26. B. P. Tinkham, D. A. Walko, M. J. Bedzyk, *Phys. Rev. B* **67**, 035404-1-6 (2003).
27. K. Shull, A. Kellock, *J. Polym. Sci. B* **33**, 1417 (1995).
28. E. T. Ogama *et al.*, *IEEE International Reliability Physics Symposium, 40th Annual Proceedings* (IEEE, Piscataway, NJ, 2002), pp. 312–321.
29. R. R. Keller, C. E. Kalnas, J. M. Phelps, *J. Appl. Phys.* **86**, 1167 (1999).
30. E. Nagao, O. Kaneko, J. A. Dvorak, *J. Struct. Biol.* **130**, 34 (2000).
31. K. Haldar, M. A. Ferguson, *J. Biol. Chem.* **260**, 4969 (1985).
32. D. Gaur, D. C. Ghislaine, L. H. Miller, *Int. J. Parasitol.* **34**, 1413 (2004).

33. Supported by NSF Major Research Instrumentation grant DMR-0420923, NSF Nanoscale Science and Engineering Center grant EEC-0118025, and based on U.S. Department of Energy Basic Energy Sciences grant DE-FG02-92ER45475. This work made use of the NU*ANCE* center facilities at Northwestern University. We thank K. Shull and A. Hagman for polymer-nanoparticle samples, and K. Haldar and her group for assistance with the malaria-infected RBCs.

20 July 2005; accepted 22 August 2005
10.1126/science.1117694

A 5-Micron-Bright Spot on Titan: Evidence for Surface Diversity

Jason W. Barnes,[1]* Robert H. Brown,[1] Elizabeth P. Turtle,[1] Alfred S. McEwen,[1] Ralph D. Lorenz,[1] Michael Janssen,[2] Emily L. Schaller,[3] Michael E. Brown,[3] Bonnie J. Buratti,[2] Christophe Sotin,[4] Caitlin Griffith,[1] Roger Clark,[5] Jason Perry,[1] Stephanie Fussner,[1] John Barbara,[6] Richard West,[2] Charles Elachi,[2] Antonin H. Bouchez,[7] Henry G. Roe,[3] Kevin H. Baines,[2] Giancarlo Bellucci,[8] Jean-Pierre Bibring,[9] Fabrizio Capaccioni,[10] Priscilla Cerroni,[10] Michel Combes,[11] Angioletta Coradini,[8] Dale P. Cruikshank,[12] Pierre Drossart,[11] Vittorio Formisano,[8] Ralf Jaumann,[13] Yves Langevin,[9] Dennis L. Matson,[2] Thomas B. McCord,[14] Phillip D. Nicholson,[15] Bruno Sicardy[11]

Observations from the Cassini Visual and Infrared Mapping Spectrometer show an anomalously bright spot on Titan located at 80°W and 20°S. This area is bright in reflected light at all observed wavelengths, but is most noticeable at 5 microns. The spot is associated with a surface albedo feature identified in images taken by the Cassini Imaging Science Subsystem. We discuss various hypotheses about the source of the spot, reaching the conclusion that the spot is probably due to variation in surface composition, perhaps associated with recent geophysical phenomena.

Large-scale relatively bright and dark regions are present on Titan's surface. Two bright areas particularly stand out: the continent-sized Xanadu Regio centered at 110°W, 15°S and the sub-Saturnian mid-south-latitude bright region (now provisionally named "Tsegihi")